Precision measurement of subcontinuum gas conduction within microconfinements

Greg I. Acosta ⬤, Malachi Hood ⬤, and Mohammad Ghashami ⬤*

Mechanical and Materials Engineering Department, University of Nebraska-Lincoln, Lincoln, Nebraska 68588, USA

Subcontinuum gas conduction is an essentially important phenomenon in disparate fields of applications ranging from aerospace vehicles to biomedical sensors, and has been the focus of many computational studies over the past decades. These studies predicted that the energy exchange mechanisms are driven by gas-surface interactions, strongly dependent on the gas and surface characteristics. Despite its fundamental and practical importance, thermal transport via gas conduction at noncontinuum regimes mostly remains experimentally unverified. Here, we report precision measurements of subcontinuum gas conduction within parallel microcavities and elucidate its dependence on the gas and surface characteristics. More importantly, we demonstrate a systematic approach for extracting the energy accommodation coefficient (EAC), which is necessary to establish gas-surface scattering kernels or develop diffusive-specular solutions to the Boltzmann transport equation. EACs are also required for calculating the temperature jump coefficient in near-continuum conditions to solve classical hydrodynamical equations. We show a correction to the kinetic theory in the transition to near-continuum regimes (particularly for nonmonatomic gases) by extracting a physical parameter representing the intermolecular collisions within the Knudsen layer. Our results agree well with the kinetic theory predictions and are expected to inform the development of technologies such as thermal switches, gas sensors, and light-driven actuators.

Conductive heat transfer through rarefied gases is a classical and fundamentally important problem in many engineering applications, including thermal insulation of spacecrafts [1–3], gas sensors [4–6], microgas chromatography [7,8], heat pumps [9–13], combustors [14–17], optical/photophoretic actuators [18–22], and nano-electromechanical systems [23–29]. In such systems, the length scale (L) is usually smaller than the molecular mean free path of the gas (λ), leading to large Knudsen numbers ($Kn = \lambda/L$). At $Kn > 1$, the gas is in a nonequilibrium state which makes the thermal transport process dictated by the gas-surface interactions (GSIs) [30]. Despite the critical implications of rarefied gas conduction, the experimental study of such transport phenomenon has remained very limited [31–35]. Understanding GSIs is inherently complex due to a vast interconnected parameter space associated with gas type, surface material and morphology, surface and gas temperatures, and adsorption susceptibility [36,37]. To represent the net effect of GSIs, the energy accommodation coefficient (EAC) is commonly used, $\alpha = \Delta E_i / \Delta E_{max}$, where ΔE_i is the energy that incident gas molecules gain after colliding with the surface, and ΔE_{max} is the maximum energy attainable from the GSI [38]. EACs are of significant importance in the kinetic modeling of heat transfer problems using the Boltzmann transport equation (BTE) by providing boundary conditions in the form of temperature

jump coefficient for near-continuum conditions [39–41], or obtaining scattering kernels for GSIs [42–44].

Obtaining EACs has been the subject of theoretical [45,46], numerical [47–52], and experimental studies [31–33,35,53–56]. While the theoretical studies of EAC strongly rely on the available experimental data for verification and improvement, the measurements have been limited to monatomic and a few polyatomic gases (e.g., N_2 and CO_2) within ideal confinements. Most of the EAC measurements were conducted using the concentric cylinder apparatus [57–61], which, although simple, could not test different materials or surface structures. To circumvent this limitation, experiments with parallel plate configurations were employed [32,34,62]. However, establishing a (micrometer) parallel gap distance and accurately measuring heat fluxes at low pressures has proven challenging, impeding its extensive use.

In this letter, we report direct and systematic measurements of subcontinuum gas conduction heat transfer for monatomic, diatomic, and polyatomic gases between planar structures. We demonstrate accurate extraction of EACs for smooth and functionalized surfaces from the subcontinuum conduction measurements. Furthermore, we express a measurement-driven correction factor to the simple kinetic theory in the transition and near-continuum regimes to account for the inter-molecular collisions within the Knudsen layer [39,63–66]. To this end, we have developed a versatile experimental platform [see Fig. 1(a)] where two planar samples are mounted with an overlap area of 5×5 mm^2. The bottom stage has a heater (Watlow 8×8 mm^2) and a resistance temperature detector (RTD) attached to the heat spreader. The top sample is placed on a 4.4×4.4 mm^2 heat flux sensor (gSKIN-XM greenTEG) with a response time of 0.7 s and an accuracy of $\pm 3\%$. A thermoelectric cooler (TEC)
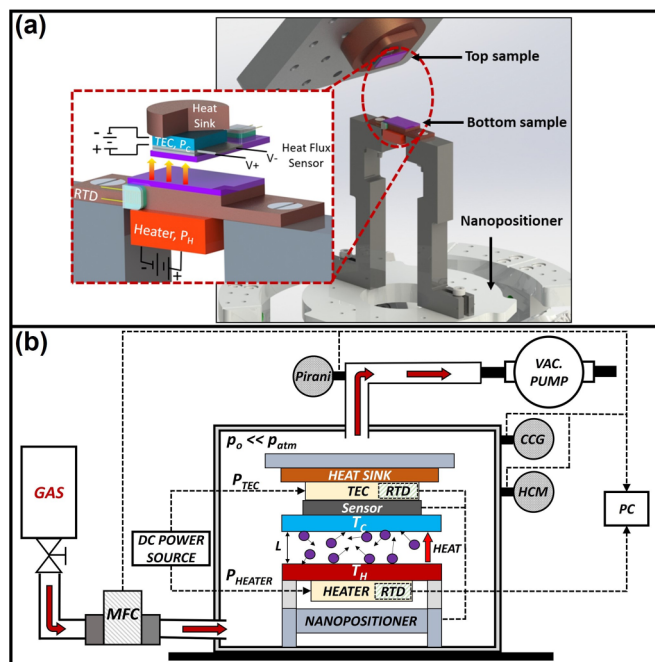
*mghashami2@unl.edu

FIG. 1. Schematic illustrations of the experimental setup for precision measurement of subcontinuum gas conduction. (a) Developed nanopositioner platform and the inverted breadboard where $10 \times 5\,\mathrm{mm}^2$ samples are mounted perpendicularly. The inset shows the arrangement of the sample assemblies. (b) Vacuum chamber housing the setup, equipped with MFC and a VAT valve to precisely maintain the gas pressure.
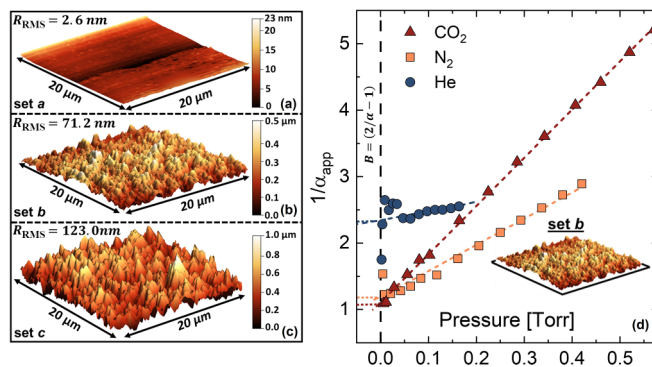

FIG. 2. (a)–(c) AFM surface morphology and the measured roughness of the three sets of Si samples. All AFM scans were generated using tapping mode with a Si probe tip, with a resonant frequency of 260 kHz. (d) EAC extraction from heat flux measurements corresponding to He, N_2 and CO_2, confined by samples of set b with a gap distance of $L = 500\,\mu\mathrm{m}$.

controls the top sample's temperature. RTDs are connected to NI cDAQ-9171 to maintain a steady temperature by feedback controlling the power to the heater and TEC. To accurately control the relative position of the two surfaces, the top stage is fixed while the bottom stage is placed on a nanopositioner with 1- nm translational resolution in all directions and $1 - \mu\mathrm{m}$ rotational resolution. Using this nanopositioner enables precise control of the gap distance between the samples, allowing us to reach different thermal transport regimes [67]. As shown in Fig. 1(b), the setup is housed in a high-vacuum chamber equipped with a VAT gate valve. A gas supply line is connected to the chamber via a mass-flow-controller (MFC), enabling precise pressure control. By adjusting the mass flow rate of the gas from $0 - 5$ SCCM, we can maintain steady gas pressures ranging from $0.005 - 0.5$ Torr.

For any measurement scenario, the heat transfer between the two samples measured by the heat flux sensor (Q_{Meas}) can consist of two main mechanisms, thermal conduction via gas molecules (Q_{Gas}) and thermal radiation (Q_{Rad}), yielding $Q_{\mathrm{Meas}} = Q_{\mathrm{Gas}} + Q_{\mathrm{Rad}}$. Thus, as a preliminary step to measuring Q_{Gas}, we must measure the radiative heat transfer, Q_{Rad}, at high-vacuum conditions. Q_{Rad} consists of the thermal radiation directly exchanged between the samples and the background thermal radiation. Before any measurements, a parallelism alignment between the two samples is performed to establish a precise gap distance (see Appendix B). After alignment, to measure Q_{Rad}, we fully retract the samples and set $T_{\mathrm{H}} = 50^{\circ}$C and $T_{\mathrm{C}} = 23^{\circ}$C, while the pressure is below 10^{-6} Torr. Once steady, we measure the heat flux by varying

the distance from 750 to 5 µm in decremental steps while feedback controlling the temperatures.

To measure Q_{Gas}, we fully retract the samples to 750 µm while the temperatures are still fixed. We set the pressure to 0.5 Torr by adjusting the outflow through the VAT valve and controlling the inlet gas flow rate via MFC. Once steady, we record the heat flux and pressure for about 5 min. At the same gap, we gradually reduce the gas flow rate to establish lower pressures down to 3.5×10^{-3} Torr. The same procedure is repeated for smaller gaps down to 5 µm. It is noteworthy that for the measurements at lower gaps, we always initialize with a gap of 750 µm and then approach the samples to the desired distance. This ensures gas particles can occupy the space between the samples, especially at lower pressures.

To fully capture the central role of surface characteristics in the energy exchange process through GSI, we used the laser-induced periodic surface structuring (LIPSS) technique to fabricate surface structures in a well-controlled manner. Briefly, LIPSS can generate highly reproducible micro/nanoscale quasiperiodic structures formed due to light-matter interactions between incident ultrashort laser and surface waves that propagate or scatter at the surface of the irradiated material. By modulating the intensity or scanning velocity of the focused laser, one can control the periodicity and the height of the structures ranging from several nanometers to a few micrometers [68–70]. In this work, we studied three different sets of samples, all diced out of an N-doped silicon (Si) wafer, with an average resistivity of 1.2 Ω cm and a crystal orientation of {111}. Samples of set a were unmodified to serve as our baseline for comparison to the literature. Samples of sets b and c were fabricated using LIPSS with different raster speeds [71] (see Appendix A). Figure 2 shows the surface morphology of these three sets captured by atomic force microscopy (AFM). As shown, a root-mean-square roughness (R_{RMS}) of 2.6 nm was measured for set a, while for the LIPSS samples of sets b and c, R_{RMS} of 71.2 nm and 123 nm were measured, respectively. After fabrication, a cleaning protocol was carried out to remove any surface contaminations [72] (see Appendix A).

TABLE I. EACs of sample sets for He, N_2 and CO_2.

Sample	R_{RMS}	α_{He}	α_{N_2}	α_{CO_2}
Set a	2.6 nm	0.50 ± 0.03	0.87 ± 0.04	0.97 ± 0.05
Set b	71.2 nm	0.61 ± 0.05	0.94 ± 0.06	0.97 ± 0.05
Set c	123.0 nm	0.67 ± 0.02	0.99 ± 0.08	0.99 ± 0.01

The EAC for a particular surface can be determined by measuring the gas conduction heat flux at very low pressures. This technique, known as the low-pressure (LP) method [73], requires the measurement of gas conduction at or near the free-molecular regime to minimize the uncertainties due to particle-particle collisions. In that case, EAC can be obtained as the ratio between the measured heat flux (Q_{Meas}) and the theoretical free-molecular heat flux for a fully accommodating surface ($Q_{FM,\alpha=1}$), i.e., $Q_{Meas}/Q_{FM,\alpha=1}$ [73–75]. However, measuring heat flux at the deep free-molecular regime might be challenging due to the scarce presence of gas particles, which leads to a weak signal hardly detectable by the heat flux sensor. Therefore, to account for the deviation from purely free-molecular conditions, a different term known as the "apparent EAC" is used that can be represented as [76],

$$\alpha_{app} = \frac{Q_{Meas}}{Q_{FM,\alpha=1}} = \frac{q^*}{1 + q^*\left[\left(\frac{1-\alpha_1}{\alpha_1}\right) + \left(\frac{1-\alpha_2}{\alpha_2}\right)\right]}. \quad (1)$$

It should be noted that α_{app} is different from the EAC. Here, $q^* = Q_{\alpha=1}/Q_{FM,\alpha=1}$ is a theoretical heat transfer coefficient, where $Q_{\alpha=1}$ is the theoretical gas conduction heat flux at subcontinuum transport regime for a fully accommodating case [59]. α_1 and α_2 are the EACs for the two surfaces, and if identical, $\alpha_1 = \alpha_2 = \alpha$. In this case, to extract EAC, we can rewrite Eq. (1) in a linear form,

$$\frac{1}{\alpha_{app}} = \frac{1 - q^*}{q^*} + \left(\frac{2}{\alpha} - 1\right) = A(P) + B, \quad (2)$$

where $A(P)$ varies with pressure and B is the intercept. At highly rarefied conditions, $q^* = 1$ which yields $\alpha_{app} = \alpha/(2 - \alpha)$. Using this factor, the theoretical free-molecular heat flux expression can be given as [77],

$$Q_{FM} = \frac{\alpha}{(2 - \alpha)} \frac{(\gamma + 1)c_v P(T_H - T_C)}{\sqrt{8\pi R T_{FM}}}, \quad (3)$$

where γ is the specific heat ratio, c_v is the specific heat capacity at constant volume, R is the specific gas constant, and T_{FM} is the effective mean temperature of the gas in the free-molecular regime.

Figure 2(d) shows the linear dependence of $1/\alpha_{app}$ on pressure for He, N_2, and CO_2 gases with samples of set b while separated by $L = 500\,\mu m$. A simple linear least lquare regression is performed to obtain the intercept $B = (2/\alpha - 1)$. The extracted EACs for all surfaces are shown in Table I. While the values for He and N_2 on smooth Si surfaces agree with the prior experiments [32], there is no literature—to our knowledge—either on the nonsmooth Si surfaces or for the CO_2 gas. For a given surface, the EAC increases with an increase in the molecular weight and structure of the interacting gas [38,57]. Expectedly, an increase in surface roughness
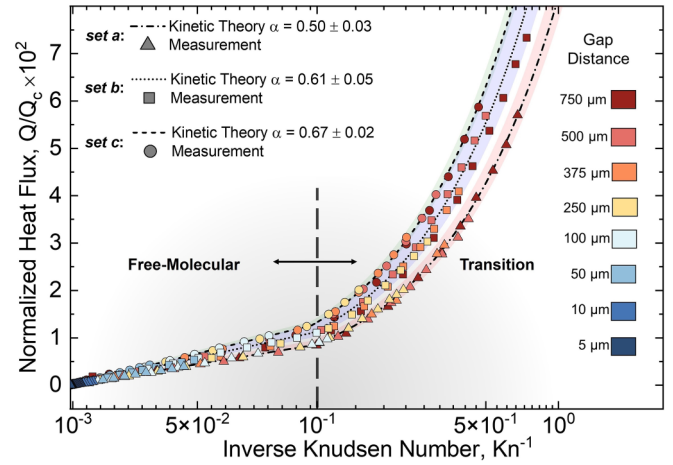

FIG. 3. Measured heat flux in the transition and free-molecular regimes for He confined by samples of sets a, b, and c, compared to the kinetic theory predictions using the extracted EACs. The color bands show the effects of EAC uncertainties on the kinetic theory calculations.

leads to larger EACs as it causes multiple collisions of the incident gas molecules with the surface. The impact of roughness on EAC enhancement appears to be more prominent for He [78], mainly because of its smaller monatomic structure, which makes it more susceptible to be accommodated by the added roughness [79,80]. On the contrary, EAC for CO_2 shows no change across set a and b due to the inherent nature of the gas molecule to strongly accommodate onto surfaces.

Using the extracted EACs, we can compare the gas conduction measurements with the theoretical predictions from kinetic theory by adopting the expression for the heat flux as [81],

$$Q = \frac{k(T_H - T_C)}{L\left(1 + Kn \frac{2-\alpha}{\alpha} \frac{9\gamma+1}{\gamma-1} \sqrt{\frac{T_{m,DF}}{T_{m,FM}}}\right)}, \quad (4)$$

which represents a temperature jump near the surfaces due to the ballistic gas-surface interactions, and a diffusive middle layer due to particle-particle collisions. Here, k is the thermal conductivity of the gas [77], and $T_{m,DF}$ and $T_{m,FM}$ are the effective mean temperature of the gas at diffusive and free-molecular conditions, respectively. It can be shown that Eq. (4) can also be obtained from the Sherman interpolation, $1/Q = 1/Q_C + 1/Q_{FM}$, where $Q_C = k(T_H - T_C)/L$ [82].

Figure 3 shows the measured gas conduction results for He, corresponding to sets a, b, and c, compared to the theoretical calculations from kinetic theory. The results are normalized with respect to the continuum limit heat flux (Q_C) and plotted as a function of the inverse Knudsen number to fully represent the variation of pressure and gap distance. An excellent agreement is demonstrated between the measurements and the kinetic theory predictions using the extracted EACs, across the free-molecular and transition regimes. The solution to the heat transfer within the transition regime for monatomic gases under small temperature ratios was previously obtained by solving the BTE under some simplifying assumptions, resulting in Eq. (4) [83,84]. These assumptions allowed the introduction of hard-sphere particles, justified by the simple
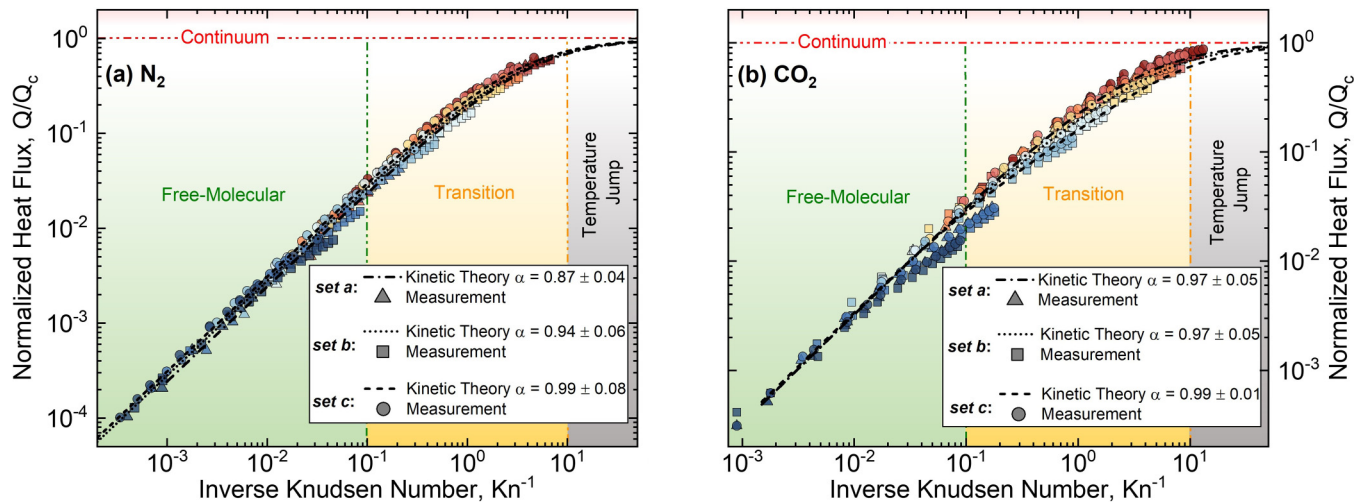
FIG. 4. Gas conduction measurements compared to the theoretical predictions from the corrected kinetic theory of Eq. (5) for (a) N_2 and (b) CO_2 across smooth and functionalized surfaces. The gap distances follow the legend in Fig. 3.

spherical molecular structure of monatomic gases, which carry only translational kinetic energy. Additionally, assuming a small temperature ratio between the gas and surface will allow linearizing the BTE by representing the velocity distribution of the gas molecules as a simple perturbation from the ideal Maxwell velocity distribution [85]. Although our measurements were performed at a temperature ratio of approximately 1.09 (calculated in degree Kelvin), it has been shown that the EAC of He will not vary with respect to the temperature ratio [57].

Figure 4 shows the measurements of sub-continuum gas conduction for N_2 and CO_2 within the three different sets of surfaces. While most of the measured data for He lies within the free-molecular regime (see Fig. 3), it is more evenly distributed for the cases of N_2 and CO_2. This is attributed to the larger mean free path (due to a smaller molecular diameter) of He compared to N_2 and CO_2 at the given pressures. Notably, at any gap distance, the measured data for N_2 and CO_2 (particularly at higher pressures) are more dispersed than the He case. This divergence roots in the discrepancy between the gas pressure measured by the transducer and the actual pressure within the two plates. Since the chamber is significantly larger than the measurement system, the local pressure of the gas confined between the two samples is slightly lower than what the pressure transducers are measuring. This deviation grows for gases with larger molecular structures, leading to a miscalculation of the Knudsen number by overestimating the mean free path (see Appendix D).

The measurements show that regardless of the gas type, the heat flux enhances by increasing the surface roughness, as expected from the extracted EACs in Table I. Comparing the results of He (as a monatomic gas) with the more complex N_2 and CO_2 gases, we observe that the heat flux increases remarkably as the size and molecular weight of the gas increase. A polyatomic gas molecule such as CO_2 can contain nine various energy modes (three translational, two rotational, and four vibrational degrees of freedom), making it a better energy carrier than He (with three translational modes) and N_2 (with three translational, two rotational, and one vibrational mode). It is noted that the contribution of vibrational modes (for both

N_2 and CO_2) is negligible due to their high characteristic vibration temperature.

While the measurements for He exhibited a great match to the kinetic theory predictions, the measured heat fluxes for N_2 and CO_2 do not agree well with the model represented by Eq. (4) (see Appendix F). As discussed earlier, Eq. (4) was derived under simplifying assumptions for monatomic gases, not applicable to more complex polyatomic gases. Moreover, Eq. (4) does not account for the particle-particle collisions in the transition regime, thus resulting in an overprediction of heat transfer. To correct the kinetic theory for polyatomic gases in the transition and near-continuum regimes, we use the modified version of Eq. (4) as below [39,63–66]:

$$Q = \frac{k(T_H - T_C)}{L\left[1 + Kn\frac{2-\alpha}{\alpha}\frac{9\gamma+1}{\gamma-1}\sqrt{\frac{T_{m,DF}}{T_{m,FM}}}\left(1 + \frac{c_1\alpha}{1+c_2Kn}\right)\right]}, \quad (5)$$

which incorporates two additional parameters, c_1 and c_2, where c_1 represents the effect of intermolecular collisions within the Knudsen layers, and c_2 helps retain the free-molecular conditions for the given theory. This correction was introduced from the solution to the temperature-jump problem for the linearized BTE, in which variational methods or discrete-ordinate methods were employed to obtain accurate solutions for the case of monatomic gases, by considering different interaction potentials [e.g., Maxwell, hard-spheres, Lennard-Jones, and n(r)-6] [64–66]. These coefficients can also be obtained from direct simulation Monte Carlo (DSMC) simulations using the above theoretical solution [63]. Nevertheless, these coefficients have never been experimentally verified or extracted from sub-continuum gas conduction measurements. To obtain c_1 and c_2, we employ a nonlinear regression, where the dependent variable is the natural logarithmic of the heat flux data, and the independent variables are the extracted EACs and the natural logarithmic of the Knudsen number [63] (see Appendix F). The obtained c_1 coefficients are 0.116 for He, 0.148 for N_2, and 0.863 for CO_2, while the coefficient c_2 was fixed to 0.599 for all gases. The results for the corrected kinetic theory using Eq. (5) are shown in Fig. 4, demonstrating good agreement with the measurements

for both N_2 and CO_2. Although the correction for He was not necessary, we expect that if the measurements were conducted near the continuum limit, deviations from the kinetic theory of Eq. (4) would be observed [39,63–66]. The correction coefficients reported here are experimentally determined are of significant importance for calculating temperature jump coefficient in BTE for any gas-solid system [86,87].

To conclude, we performed systematic measurements to provide an unprecedented experimental demonstration of subcontinuum gas conduction beyond monatomic gases across smooth and laser-functionalized Si surfaces. We experimentally extracted EACs to characterize the gas-surface energy interactions accurately. Further, we showed the deviation of gas conduction measurements in the transition regime from the Sherman-Lee formula due to the strong impact of the Knudsen layer on the transport mechanism. We addressed this by using the corrected closed-form expression with coefficients derived from our measurements. The findings can shed light on the fundamental understanding of intermolecular potentials required to accurately represent particle-particle collisions in complex gas-surface problems.

APPENDIX A: SURFACE FUNCTIONALIZATION, CLEANING AND CHARACTERIZATION

Samples of sets b and c were fabricated using LIPSS with a laser fluence of 0.28 J/cm^2, pulse energy of 1050 μJ, a pitch of 160 μm, and a beam diameter of 962 μm, while rastering the samples on a motorized stage. The difference between sets b and c is caused by changing the raster speed from 11.00 to 12.25 mm/s, which decreased the pulse count from 584 to 489, respectively. For surface characterization, we employed AFM to fully map the morphology of the original (i.e., set a) and the LIPSS samples of sets b and c. A silicon-based AFM probe was used with a 2-nm tip and a resonant frequency of 260 kHz. Since the samples were relatively large, four scanning areas of 20 μm × 20 μm were randomly selected on the surface of each sample. Partial results of all the scans are shown in Fig. 5, where evenly distributed quasiperiodic nanostructures can be observed on sets b and c. From the AFM results in Fig. 5, it can be seen that LIPSS is an excellent technique for controlling the degree of surface roughness in a quasiperiodic pattern.
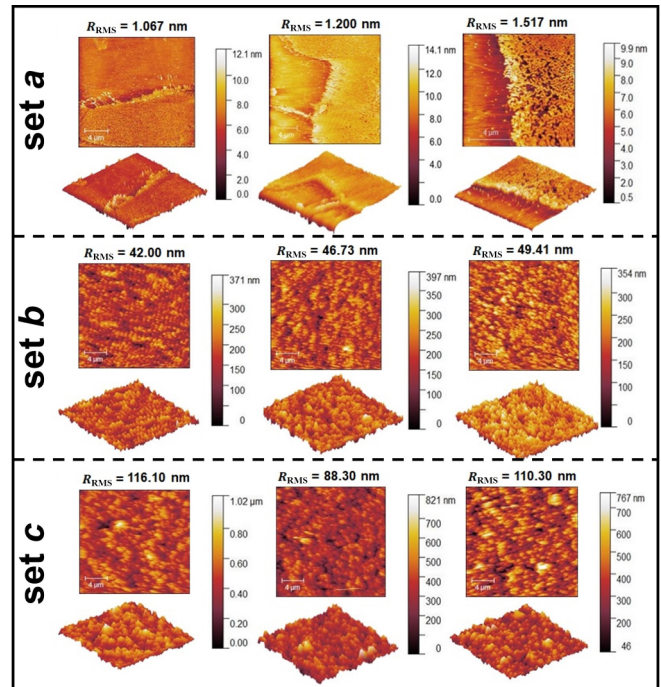

FIG. 5. Mapped surface morphology of sets a, b, and c using AFM. Sample a is unmodified, while b and c are engineered via LIPSS.

Although generating higher surface roughness was possible, we kept the maximum roughness to less than one micrometer. A highly rough surface ($R_{\rm RMS} > 1$μm) will lead to prolonged gas particles scattering at the surface, causing multiple collisions of incident molecules with the surface, hence allowing enough time to obtain fully accommodated conditions [38]. Moreover, the specific crystalline structure of the surface plane may be altered by the extended use of LIPSS, which could undesirably impact the gas-surface interactions. After fabrication, samples were cleaned in an ultrasonic bath and dried with nitrogen. Next, a special optics-cleaning polymer (First Contact) was applied to remove any remaining surface debris. Finally, samples were placed inside a deep ultraviolet (UV) ozone cleaner (Novascan, PSD-UV4) for 30 min to remove any organic contamination.

APPENDIX B: ALIGNMENT OF SAMPLES

After cleaning, samples are fixed to the top and bottom stages of the measurement system, as shown in Fig. 1 of the main text. Initially, samples are manually aligned by first fixing the nanopositioner to the designated marks on the floor of the vacuum chamber and then placing the top stage (with the inverted breadboard) directly above that. The optical breadboard is manually shifted until the edges of the samples are perfectly aligned, and an overlap area of 5 × 5 mm^2 is obtained. Once positioned, the nanopositioner adjusts the bottom sample to match the top sample's angular orientation. An Allied Vision 1800–2050m microscopic camera (Fig. 6) is used to help with adjusting the translational displacement and rotational angles in the x and y directions, as shown in Fig. 7. Using the camera, together with MATLAB's Image
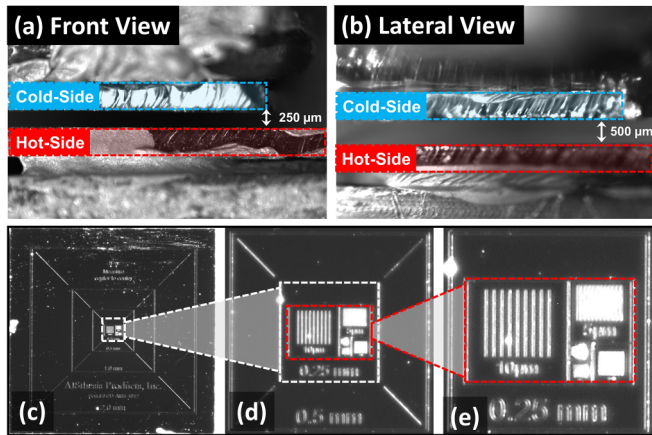
FIG. 6. Microscopic images captured by a 20 MP high-resolution camera, equipped with a $2\times$ objective lens. (a) Front view of the samples separated by 250 μm. (b) Lateral view of the samples, separated by 500 μm. (c) 2×2 mm^2 image of an AFM calibration slide with patterned surface features, ranging from 2 mm to 1 μm. (d) 0.5×0.5 mm^2 zoomed-in section of the AFM slide. (e) 0.25×0.25 mm^2 zoomed-in section, where 10 μm features are clearly distinguishable.

Acquisition toolbox, we can estimate the distance between any two points based on the pixel resolution of the camera 5496 (horizontal) $\times 3672$ (vertical), with a pixel size of 2.4 μm (horizontal) $\times 2.4$ μm (vertical). Since the camera is equipped with a $2\times$ objective lens, this yields a sensing area of approximately 6.6×4.4 mm^2. For the next step of the alignment, we pump down the chamber until high-vacuum conditions (1×10^{-6} Torr) is obtained. At this point, we set the bottom sample to a temperature of $T_H = 50\,°C$, while the top sample's

FIG. 7. Illustration of the angular alignment of the rotational angle (a) θ_y and (b) θ_x of the samples. (c) Displacement of the nanopositioner in the z direction. Here the total travel is approximately 2 μm until reaching the contact point. (d) Temperature signal and (e) heat flux signal originating from the cold side sample. Temperature slightly rises until a jump is observed, reaching $T_{cont.} = 27.5\,°C$. The observed temperature jump corresponds to a heat flux jump, where the heat transfer mode switches from radiation to conduction.

temperature is not fixed. We approach the samples by moving the bottom sample in increments of 50 μm in the z direction until a contact between the two samples is observed as a sudden temperature jump of the top sample. At this point, the samples are retracted for approximately 10 μm, and the approaching process is repeated with finer increments until a gap distance of approximately 2 μm is established, as in Fig. 7(c). Now, the rotational angles θ_x and θ_y are readjusted by keeping one angle fixed while changing the other in increments of 0.050 degrees until the edge of the bottom sample touches the top sample, leading to a temperature jump of the top sample. This process is repeated to find the second contact angle in the opposite direction. The median of the two found angles will provide the best angular parallelism between the two samples. To facilitate the tedious process of angular alignment, this procedure has been automated to find the optimal angles that give us the best parallelism between the two sides.

APPENDIX C: BACKGROUND GAS CONDUCTION

In our measurement system, the heat transfer between the two samples, measured by the heat flux sensor (Q_{Meas}) can consist of two primary mechanisms, thermal conduction by the gas molecules (Q_{Gas}) and thermal radiation heat transfer (Q_{Rad}),

$$Q_{\mathrm{Meas}} = Q_{\mathrm{Gas}} + Q_{\mathrm{Rad.}} \tag{C1}$$

To fully characterize the potential contributions of other sources to the measured heat flux, a series of experiments were carried out that are discussed in detail in the following subsections.

For Q_{Gas} in Eq. (C1), special consideration of other potential thermal sources that might have exchanged energy with the gas molecules must be taken into account. For example, gas particles are exposed to other surfaces, such as the nanopositioning stage and the TEC's heat sink, with different temperatures than the samples. So, these gas molecules might gain thermal energy from these surfaces that the heat flux sensor could undesirably still pick up. Therefore, as a precursor to our measurements, we needed to account for this background gas conduction that is not originated from the interactions between gas molecules and the hot sample. We considered three possible scenarios to test whether the influence of the background gas conduction would contribute to the total heat transfer. In the first scenario, we completely disabled the TEC and heater while keeping the nanopositioner on. Here, we measured the heat flux exchanged between the samples separated by a gap of 500 μm while varying the pressure of N_2 gas. As shown in Fig. 8(a), the results demonstrate that the measured heat flux increased with pressure.

Although small, this suggests that the gas particles are gaining thermal energy from the surfaces of the nanopositioner (i.e., its piezoactuators). However, once the heater is activated, similar to the real experiment, the concentration of gas molecules in the vicinity of the heater will likely be in thermal equilibrium with the respective temperature of the heater. To understand this, let us consider, for example, CO_2 at a pressure of 0.5 Torr, which yields a mean free path of about 70 μm. In this case, there will be a large number of CO_2 gas molecules (approximately 4.5×10^{20}) inside the chamber,
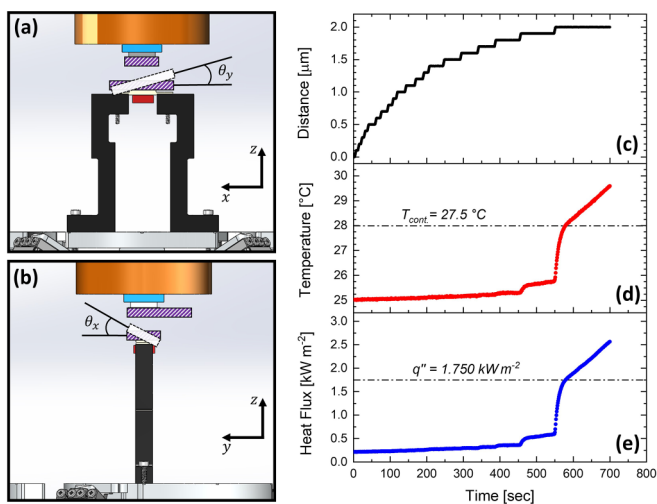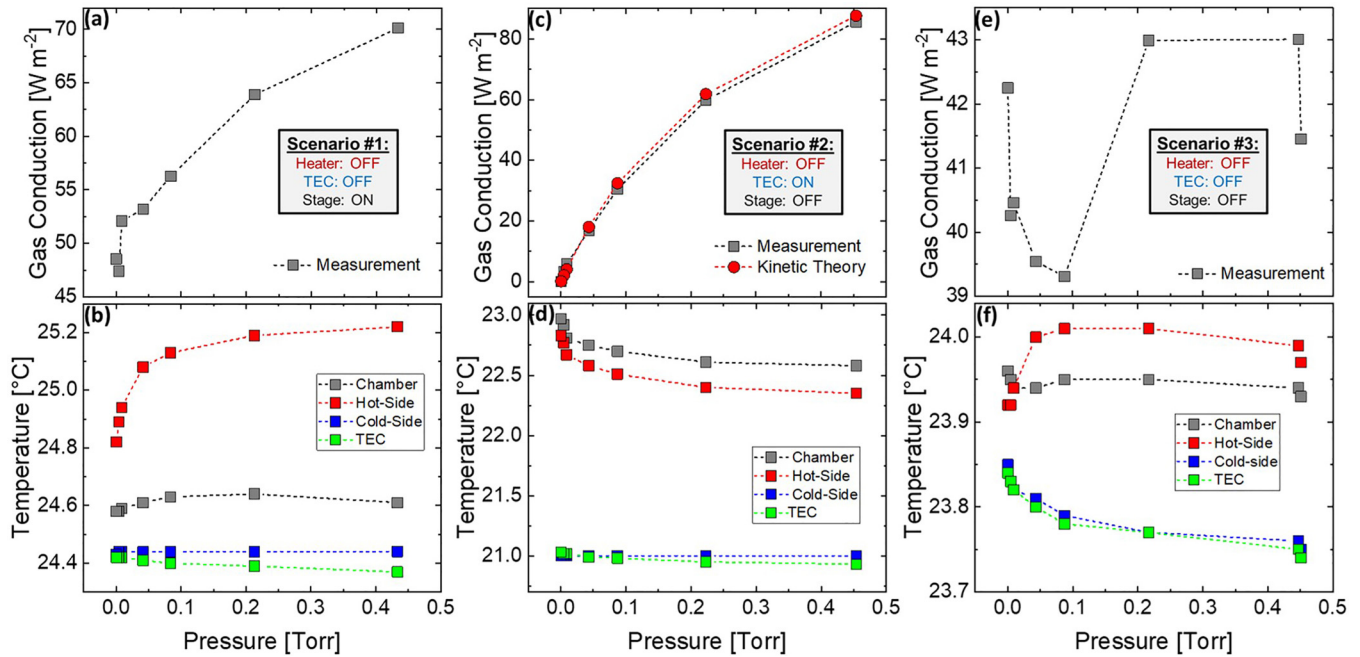
FIG. 8. (a) Measured heat flux as a function of pressure for scenario one where the TEC and heater were completely deactivated, but the nanopositioner was on. (b) Temperature variation of the chamber, hot-side, cold-side, and TEC by pressure, for scenario one. In scenario one, the increase in heat flux and temperature of the hot side suggests that the nanopositioning stage delivers thermal energy to the surrounding gas. (c) Measured and calculated heat flux for scenario two with TEC on and the heater and the nanopositioner off. The cold-side temperature was set to 21 °C. (d) Variation of the chamber, hot-side, cold-side, and TEC temperatures as a function of pressure for scenario two. (e) Measured heat flux for scenario three with the TEC, heater, and nanopositioning stage deactivated. (f) Variation of the chamber, hot-side, cold-side, and TEC temperatures as a function of pressure for scenario three. The results for all scenarios are for N_2 gas confined by set b, at a gap distance of 500 μm.

where most of these will be in thermal equilibrium with the chamber walls (maintained about room temperature). Since the sample assembly is far from the chamber walls and the nanopositioner, the gas molecules around the hot sample will likely be in thermal equilibrium with its temperature, thus not being much affected by the surface temperature of the nanopositioner when the heater is on. For the second scenario, we wanted to investigate the effect of the TEC (i.e., its hot side) on the parasitic heating of the gas molecules. To this aim, we feedback control the temperature of the cold side sample to $T_C = 21$ °C while the heater and nanopositioner are entirely disabled. The heat flux was measured for the same gas, pressures, and gap distance as in the first scenario. Here, we were limited to a temperature of 21 °C due to an unavoidable small amount of current that the TEC draws once the power source is activated. As a result, it will automatically start cooling down to a temperature below 23 °C. Additionally, since the nanopositioner is deactivated, the initial temperature of the chamber slightly dropped to approximately 23 °C, as compared to the first scenario, leading to a lower initial temperature of the top stage. The results for the second scenario are shown in Fig. 8(c), where the heat flux increased by increasing the pressure.

This increase can be attributed to a substantial temperature gradient between the cold-side sample (attached to the heat flux sensor) and the gas, as illustrated in Fig. 8(d), and does not add any undesired background conduction in our real test where the gas and the cold side temperatures are very close. To prove this, if we assume the mean temperature of the gas

is 24 °C and calculate the heat transfer by kinetic theory (for a fully accommodating case), we can obtain an excellent match between the measured data and the theoretical prediction, as depicted in Fig. 8(c).

Finally, for the last scenario, we wanted to explore if any other unaccounted thermal source might interfere with our tests. To check this, we measured the heat flux by completely disabling the TEC, heater, and nanopositioning stage. It was found that there was no variation in the heat flux as a function of pressure, suggesting that the gas temperature before entering the chamber is in thermal equilibrium with the outside ambient (i.e., room) temperature. These results are shown in Fig. 8(e), where it can also be seen that the temperature inside the chamber is approximately 24 °C, confirming our assumption for the mean temperature of the gas.

APPENDIX D: EFFECTIVE PRESSURE WITHIN THE MICROCONFINEMENT

The pressure of the rarefied gases plays a central role in the current measurements of heat conduction and its comparison to the theoretical predictions. Since the pressure of the confined gas within the two sides cannot be directly measured, we have used the readings from the sensitive pressure transducers in the chamber. To test the extent of the mismatch between the gas pressure measured by the transducer and the actual pressure within the two plates, a five-day test was carried out to observe the effect of allowing CO_2 gas particles to penetrate the confined space between the samples. Figure 9 shows the
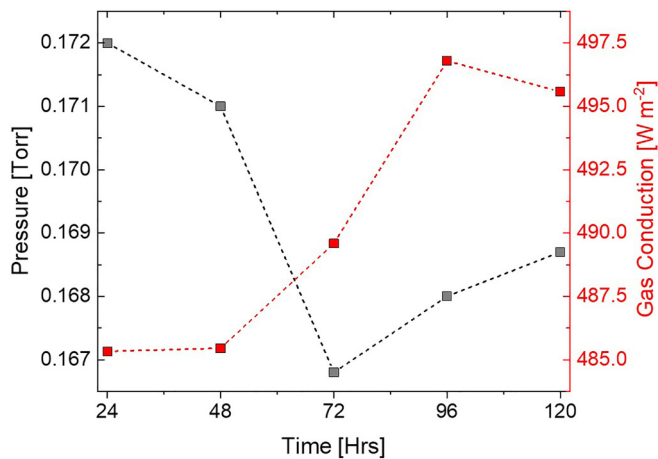
FIG. 9. Pressure and heat flux measured over five days for a fixed flow rate of CO_2 confined by set a. On day 1, the pressure was 0.172 Torr, and a heat flux of 485.33 W/m^2 was measured, showing a relative error of 4.05% compared to the calculated heat flux from kinetic theory for the same pressure. On day 5, the pressure was 0.168 Torr, and a heat flux of 495.58 W/m^2 was measured, showing a relative error of 0.67% compared to theory.

measured results for CO_2 gas confined by set a, for an established gap distance of 250 μm. The results show that as time progressed, the pressure measured by the transducer slightly dropped for the same inlet flow rate of 1.50 SCCM, while the measured heat flux slightly increased. This observed effect suggests that localized pressure between the samples reaches a more complete equilibrium condition over time by allowing more gas particles to penetrate the micro-cavity between the two sides. The increase in the total number of gas particles confined within the volumetric space then leads to a slightly

larger heat flux. The insignificant change in the heat flux suggests that the pressure mismatch is negligible. It should also be noted that to mitigate this effect further, we initialize all measurements (regardless of pressure and the desired gap) from the largest possible separation distance of 750 μm.

APPENDIX E: FAR-FIELD THERMAL RADIATION

In Eq. (C1), the term Q_{Rad} is the thermal radiation contribution from all potential emitting surfaces. In general, we can consider Q_{Rad} to consist of thermal radiation from the hot sample, Q_s, and thermal radiation from the background (i.e., experimental setup and the chamber walls), Q_b, yielding $Q_{Rad} = Q_s + Q_b$. As described in the main text, prior to the gas conduction measurements, Q_{Rad} was measured at high-vacuum conditions to be subtracted later from the total heat flux measurements when gases are introduced. While Q_b was invariable for all cases, we wanted to explore if Q_s would vary due to the added surface roughness on the LIPSS samples. To this aim, we measured Q_{Rad} across sets a, b, and c for gap distance ranging from 750 μm to 5 μm. Here a far-field value of approximately 109 W/m^2 was measured and found that there was no variation across all sample sets. To verify this observation, we calculated the thermal radiation based on the fluctuation-dissipation theorem and effective medium theory between two silicon plates for various RMS roughnesses of 10, 45, and 125 nm, subjected to a temperature of 50 °C and 23 °C for the emitter and receiver, respectively. Figure 10(a) depicts the calculated results for the thermal radiation in the near-field and far-field regimes as a function of the gap distance. Here the gap distance is defined as $d_{RMS} = d_{top} + 2 \times (3\sigma - \sigma)$, where d_{top} is the distance between opposing maximum peaks on the surface and σ is the RMS roughness of the surface [88]. It can be seen that the far-field radiation
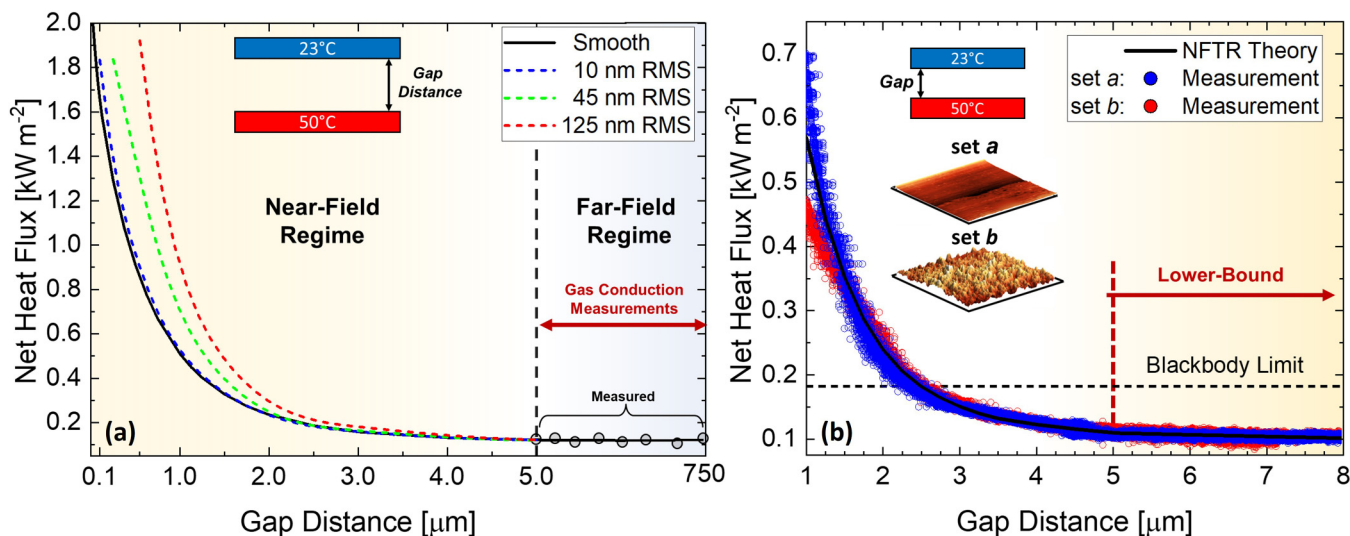

FIG. 10. (a) Effects of surface roughness on the thermal radiation exchanged between two parallel Si plates as a function of gap distance. The calculations were carried out for an RMS roughness of 10, 45, and 125 nm. From the results, surface roughness does not affect the far-field thermal radiation, which is where our gas conduction measurements are conducted. (b) Measurement of near-field thermal radiation between samples of set a and set b, for a varying gap distance of 8 μm to 1 μm. From the measured results, near-field thermal radiation will not contribute to our gas conduction measurements performed at gaps larger than 5 μm. Therefore, the lower bound of our gas conduction measurements will be the far-field thermal radiation.
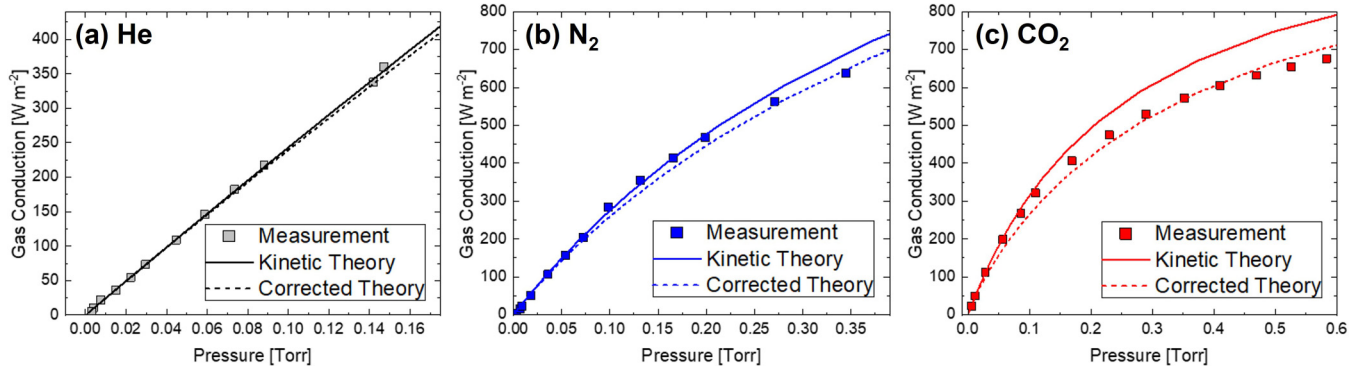
FIG. 11. Comparison between the measurements and the theoretical predictions of kinetic theory with and without the correction coefficients. The results are for He, N_2 and CO_2, confined by samples of set a, at a gap distance of 375 μm.

will not be affected by the surface roughness, where all of our gas conduction measurements are conducted. On the contrary, in the near-field regime, an increase in the RMS roughness will enhance heat flux due to the scattering of additional surface modes within the rough surface [89]. To elucidate the potential contribution of near-field thermal radiation to our heat transfer measurements at high-vacuum conditions, we performed a series of thermal radiation measurements for samples of sets a and b. By varying the gap distance from 8 μm to 1 μm in steps of 50 nm every 5 min, we recorded the heat transfer exchanged between the two samples. Fig. 10(b) depicts the measured results, showing that after 3 μm, the heat transfer is substantially enhanced due to the contribution from evanescent waves. Since our gas conduction measurements are conducted for the gap distances within the range of $5 - 750$ μm, near-field thermal radiation will not contribute to our measurements, and our lower bound of heat transfer will be the far-field thermal radiation.

APPENDIX F: KINETIC THEORY CORRECTIONS

To correct the kinetic theory for nonmonatomic gases in the transition and near-continuum regime, the following modified expression for the conductive heat flux was employed [39,63–66],

$$Q = \frac{k(T_H - T_C)}{L\left[1 + Kn\,\frac{2-\alpha}{\alpha}\,\frac{9\gamma+1}{\gamma-1}\sqrt{\frac{T_{m,DF}}{T_{m,FM}}}\left(1 + \frac{c_1\alpha}{1+c_2Kn}\right)\right]}. \quad \text{(F1)}$$

Here, the coefficient c_1 represents the effect of molecular collisions within the Knudsen layer, while c_2 is a parameter that serves to retain the free-molecular conditions for high Knudsen numbers. To obtain the correcting coefficients, a simple nonlinear regression was employed using MATLAB, where the dependent and independent variables are the heat flux and Knudsen number (a function of pressure), respectively. The measured heat flux data and the extracted EAC values for sets a, b, and c were utilized to conduct the regression. Finding c_1 and c_2 requires that the least-square error between the normalized heat flux values predicted by Eq. (F1) and experimental data are minimized [63],

$$S = \sum \left(\frac{Q}{Q_{\text{Meas}}} - 1\right)^2. \quad \text{(F2)}$$

After minimizing Eq. (F2), the extracted c_1 coefficients are: 0.116 for He, 0.148 for N_2, and 0.863 for CO_2. The c_1 value for He matches the previous theoretical calculations [64–66] extracted from the solution of Boltzmann transport equation and the numerical extraction via DSMC [63]. However, there are no experimental, theoretical or numerical studies to confirm the values of N_2 and CO_2. It is important to note that although c_2 was extracted, for the calculations, it was fixed to 0.599 to help retain the free-molecular conditions. The corrected theoretical results for He, N_2 and CO_2, confined by set a, at a gap distance of 375 μm are shown in Fig. 11.

[1] O. Uyanna and H. Najafi, Thermal protection systems for space vehicles: A review on technology development, current challenges and future prospects, Acta Astronaut. **176**, 341 (2020).

[2] S. Xiong, Y. Yang, S. Zhang, Y. Xiao, H. Ji, Z. Yang, and F. Ding, Nanoporous polybenzoxazine aerogels for thermally insulating and self-extinguishing materials in aerospace applications, ACS Appl. Nano Mater. **4**, 7280 (2021).

[3] P. Meti, D. B. Mahadik, K.-Y. Lee, Q. Wang, K. Kanamori, Y.-D. Gong, and H.-H. Park, Overview of organic–inorganic hybrid silica aerogels: Progress and perspectives, Mater. Des. **222**, 111091 (2022).

[4] A. J. Bandodkar, I. Jeerapan, and J. Wang, Wearable chemical sensors: Present challenges and future prospects, ACS Sensors **1**, 464 (2016).

[5] R. Baron and J. Saffell, Amperometric gas sensors as a low cost emerging technology platform for air quality monitoring applications: A review, ACS Sensors **2**, 1553 (2017).

[6] S. Das and M. Pal, Review–non-invasive monitoring of human health by exhaled breath analysis: A comprehensive review, J. Electrochem. Soc. **167**, 037562 (2020).

[7] Y. Qin and Y. B. Gianchandani, A fully electronic microfabricated gas chromatograph with complementary capacitive

detectors for indoor pollutants, Microsyst. Nanoeng. **2**, 15049 (2016).

[8] P. E. Leary, B. W. Kammrath, K. J. Lattman, and G. L. Beals, Deploying portable gas chromatography–mass spectrometry (GC-MS) to military users for the identification of toxic chemical agents in theater, Appl. Spectrosc. **73**, 841 (2019).

[9] N. K. Gupta and Y. B. Gianchandani, Thermal transpiration in mixed cellulose ester membranes: Enabling miniature, motionless gas pumps, Microporous Mesoporous Mater. **142**, 535 (2011).

[10] S. An, Y. Qin, and Y. B. Gianchandani, A monolithic high-flow Knudsen pump using vertical Al_2O_3 channels in SOI, J. Microelectromech. Syst. **24**, 1606 (2015).

[11] K. Kugimoto, Y. Hirota, T. Yamauchi, H. Yamaguchi, and T. Niimi, A novel heat pump system using a multi-stage Knudsen compressor, Int. J. Heat Mass Transf. **127**, 84 (2018).

[12] K. Kugimoto, Y. Hirota, T. Yamauchi, H. Yamaguchi, and T. Niimi, Design and demonstration of Knudsen heat pump without moving parts free from electricity, Appl. Energy **250**, 1260 (2019).

[13] X. Wang, T. Su, W. Zhang, Z. Zhang, and S. Zhang, Knudsen pumps: A review, Microsyst. Nanoeng. **6**, 26 (2020).

[14] B. Xu and Y. Ju, Concentration slip and its impact on heterogeneous combustion in a micro scale chemical reactor, Chem. Eng. Sci. **60**, 3561 (2005).

[15] Y. Ju and K. Maruta, Microscale combustion: Technology development and fundamental research, Prog. Energy Combust. Sci. **37**, 669 (2011).

[16] X. Yang, Z. He, L. Zhao, S. Dong, and H. Tan, Effect of channel diameter on the combustion and thermal behavior of a hydrogen/air premixed flame in a swirl micro-combustor, Energies **12**, 3821 (2019).

[17] A. Banerjee and D. Paul, Developments and applications of porous medium combustion: A recent review, Energy **221**, 119868 (2021).

[18] O. A. Schmidt, M. K. Garbos, T. G. Euser, and P. S. J. Russell, Reconfigurable optothermal microparticle trap in air-filled hollow-core photonic crystal fiber, Phys. Rev. Lett. **109**, 024502 (2012).

[19] V. Kara, Y.-I. Sohn, H. Atikian, V. Yakhot, M. Lončar, and K. L. Ekinci, Nanofluidics of single-crystal diamond nanomechanical resonators, Nano Lett. **15**, 8070 (2015).

[20] R. Pennetta, S. Xie, and P. S. J. Russell, Tapered glass-fiber microspike: High-Q flexural wave resonator and optically driven Knudsen pump, Phys. Rev. Lett. **117**, 273901 (2016).

[21] J. Lu, H. Yang, L. Zhou, Y. Yang, S. Luo, Q. Li, and M. Qiu, Light-induced pulling and pushing by the synergic effect of optical force and photophoretic force, Phys. Rev. Lett. **118**, 043601 (2017).

[22] M. Azadi, G. A. Popov, Z. Lu, A. G. Eskenazi, A. J. W. Bang, M. F. Campbell, H. Hu, and I. Bargatin, Controlled levitation of nanostructured thin films for sun-powered near-space flight, Sci. Adv. **7**, eabe1127 (2021).

[23] A. Passian, R. J. Warmack, T. L. Ferrell, and T. Thundat, Thermal transpiration at the microscale: A Crookes cantilever, Phys. Rev. Lett. **90**, 124503 (2003).

[24] B. Gotsmann and U. Dürig, Experimental observation of attractive and repulsive thermal forces on microcantilevers, Appl. Phys. Lett. **87**, 194102 (2005).

[25] A. Pikus, I. B. Sebastião, A. Strongrich, and A. Alexeenko, Characterization of a Knudsen force based vacuum sensor for $N_2 - H_2O$ gas mixtures, Vacuum **161**, 130 (2019).

[26] D. D. Vo, R. Moradi, M. Barzegar Gerdroodbary, and D. D. Ganji, Measurement of low-pressure Knudsen force with deflection approximation for gas detection, Res. Phys. **13**, 102257 (2019).

[27] T. Zhu and W. Ye, Origin of Knudsen forces on heated microbeams, Phys. Rev. E **82**, 036308 (2010).

[28] M. Defoort, K. J. Lulla, T. Crozes, O. Maillet, O. Bourgeois, and E. Collin, Slippage and boundary layer probed in an almost ideal gas by a nanomechanical oscillator, Phys. Rev. Lett. **113**, 136101 (2014).

[29] R. R. Gazizulin, O. Maillet, X. Zhou, A. M. Cid, O. Bourgeois, and E. Collin, Surface-induced near-field scaling in the Knudsen layer of a rarefied gas, Phys. Rev. Lett. **120**, 036802 (2018).

[30] B. J. McCoy and C. Y. Cha, Transport phenomena in the rarefied gas transition regime, Chem. Eng. Sci. **29**, 381 (1974).

[31] D. Braun and A. Frohn, Heat transfer in simple monatomic gases and in binary mixtures of monatomic gases, Int. J. Heat Mass Transf. **19**, 1329 (1976).

[32] W. M. Trott, J. N. Castañeda, J. R. Torczynski, M. A. Gallis, and D. J. Rader, An experimental assembly for precise measurement of thermal accommodation coefficients, Rev. Sci. Instrum. **82**, 035120 (2011).

[33] H. Yamaguchi, K. Kanazawa, Y. Matsuda, T. Niimi, A. Polikarpov, and I. Graur, Investigation on heat transfer between two coaxial cylinders for measurement of thermal accommodation coefficient, Phys. Fluids **24**, 062002 (2012).

[34] M. Grau, F. Völklein, A. Meier, C. Kunz, J. Heidler, and P. Woias, Method for measuring thermal accommodation coefficients of gases on thin film surfaces using a MEMS sensor structure, J. Vac. Sci. Technol., A **34**, 041601 (2016).

[35] H. Yamaguchi, J. Hosoi, Y. Matsuda, and T. Niimi, Measurement of conductive heat transfer through rarefied binary gas mixtures, Vacuum **160**, 164 (2019).

[36] M. Yang, Q. Sheng, L. Guo, H. Zhang, and G. Tang, How gas–solid interaction matters in graphene-doped silica aerogels, Langmuir **38**, 2238 (2022).

[37] T. Wu and D. Zhang, Impact of adsorption on gas transport in nanopores, Sci. Rep. **6**, 23629 (2016).

[38] F. O. Goodman, *Dynamics of Gas-Surface Scattering* (Elsevier, Amsterdam, 2012).

[39] S. K. Loyalka, C. E. Siewert, and J. R. Thomas, Jr., Temperature-jump problem with arbitrary accommodation, Phys. Fluids **21**, 854 (1978).

[40] D. A. Lockerby, J. M. Reese, D. R. Emerson, and R. W. Barber, Velocity boundary condition at solid walls in rarefied gas calculations, Phys. Rev. E **70**, 017303 (2004).

[41] N. N. Nguyen, I. Graur, P. Perrier, and S. Lorenzani, Variational derivation of thermal slip coefficients on the basis of the Boltzmann equation for hard-sphere molecules and Cercignani-Lampis boundary conditions: Comparison with experimental results, Phys. Fluids **32**, 102011 (2020).

[42] C. Cercignani, Scattering kernels for gas-surface interactions, Transp. Theory Stat. Phys. **2**, 27 (1972).

[43] Z. Wang, C. Song, F. Qin, and X. Luo, Establishing a data-based scattering kernel model for gas–solid interaction by molecular dynamics simulation, J. Fluid Mech. **928**, A34 (2021).

[44] M. Liao, Q.-D. To, C. Léonard, and W. Yang, Prediction of thermal conductance and friction coefficients at a solid-gas interface from statistical learning of collisions, Phys. Rev. E **98**, 042104 (2018).

[45] F. O. Goodman, On the theory of accommodation coefficients–IV. Simple distribution function theory of gas-solid interaction systems, J. Phys. Chem. Solids **26**, 85 (1965).

[46] I. Altman, On energy accommodation coefficient of gas molecules on metal surface at high temperatures, Surf. Sci. **698**, 121609 (2020).

[47] V. Chirita, B. A. Pailthorpe, and R. E. Collins, Non-equilibrium energy and momentum accommodation coefficients of Ar atoms scattered from Ni(001) in the thermal regime: A molecular dynamics study, Nucl. Instrum. Methods Phys. Res., Sect. B **129**, 465 (1997).

[48] N. Mateljevic, J. Kerwin, S. Roy, J. R. Schmidt, and J. C. Tully, Accommodation of gases at rough surfaces, J. Phys. Chem. C **113**, 2360 (2009).

[49] M. Khatoonabadi, N. I. Prasianakis, and J. Mantzaras, Lattice Boltzmann modeling and simulation of velocity and concentration slip effects on the catalytic reaction rate of strongly nonequimolar reactions in microflows, Phys. Rev. E **106**, 065305 (2022).

[50] K. K. Kammara, R. Kumar, A. K. Singh, and A. K. Chinnappan, Systematic direct simulation Monte Carlo approach to characterize the effects of surface roughness on accommodation coefficients, Phys. Rev. Fluids **4**, 123401 (2019).

[51] A. Tokunaga and T. Tsuruta, Nonequilibrium molecular dynamics study on energy accommodation coefficient on condensing liquid surface–Molecular boundary conditions for heat and mass transfer, Phys. Fluids **32**, 112011 (2020).

[52] S. Mohammad Nejad, E. Iype, S. Nedea, A. Frijns, and D. Smeulders, Modeling rarefied gas-solid surface interactions for Couette flow with different wall temperatures using an unsupervised machine learning technique, Phys. Rev. E **104**, 015309 (2021).

[53] A. K. Rebrov, A. A. Morozov, M. Y. Plotnikov, N. I. Timoshenko, and V. A. Maltsev, Determination of accommodation coefficients of translational and internal energy using a thin wire in a free-molecular flow, Rev. Sci. Instrum. **74**, 1103 (2003).

[54] H. Yamaguchi, T. Imai, T. Iwai, A. Kondo, Y. Matsuda, and T. Niimi, Measurement of thermal accommodation coefficients using a simplified system in a concentric sphere shells configuration, J. Vac. Sci. Technol. A **32**, 061602 (2014).

[55] F. Sharipov and M. R. Moldover, Energy accommodation coefficient extracted from acoustic resonator experiments, J. Vac. Sci. Technol. A **34**, 061604 (2016).

[56] D. Ganta, E. B. Dale, J. P. Rezac, and A. T. Rosenberger, Optical method for measuring thermal accommodation coefficients using a whispering-gallery microresonator, J. Chem. Phys. **135**, 084313 (2011).

[57] J. Kouptsidis and D. Menzel, Accommodation of the rare gases on clean tungsten surfaces between 77 and 380 K, Ber. Bunsenges. Phys. Chem. **74**, 512 (1970).

[58] B.-T. Yeh and A. Frohn, Heat conduction in binary gas mixtures between concentric cylinders, Phys. Fluids **16**, 801 (1973).

[59] L. B. Thomas, C. L. Krueger, and S. K. Loyalka, Heat transfer in rarefied gases: Critical assessments of thermal conductance and accommodation of argon in the transition regime, Phys. Fluids **31**, 2854 (1988).

[60] S. J. O'shea and R. E. Collins, An experimental study of conduction heat transfer in rarefied polyatomic gases, Int. J. Heat Mass Transf. **35**, 3431 (1992).

[61] H. Chalabi, O. Buchina, L. Saraceno, M. Lorenzini, D. Valougeorgis, and G. Morini, Experimental analysis of heat transfer between a heated wire and a rarefied gas in an annular gap with high diameter ratio, in *Journal of Physics: Conference Series*, Vol. 362 (IOP Publishing, 2012), p. 012028.

[62] D. Bayer, U. Gross, and K. Raed, A new facility for the experimental investigation on nano heat transfer between gas molecules and ceramic surfaces, in *Proceedings of the 32nd International Thermal Conductivity Conference* (Purdue University, West Lafayette, Indiana, USA, 2014).

[63] M. A. Gallis, J. R. Torczynski, and D. J. Rader, A computational investigation of noncontinuum gas-phase heat transfer between a heated microbeam and the adjacent ambient substrate, Sens. Actuators, A **134**, 57 (2007).

[64] C. E. Siewert, The linearized Boltzmann equation: A concise and accurate solution of the temperature-jump problem, J. Quant. Spectrosc. Radiat. Transfer **77**, 417 (2003).

[65] S. K. Loyalka, Temperature jump: Rigid-sphere gas with arbitrary gas/surface interaction, Nucl. Sci. Eng. **108**, 69 (1991).

[66] S. K. Loyalka, Slip and jump coefficients for rarefied gas flows: Variational results for Lennard-Jones and n(r)-6 potentials, Physica A **163**, 813 (1990).

[67] M. Ghashami, H. Geng, T. Kim, N. Iacopino, S. K. Cho, and K. Park, Precision measurement of phonon-polaritonic near-field energy transfer between macroscale planar structures under large thermal gradients, Phys. Rev. Lett. **120**, 175901 (2018).

[68] B. Dusser, Z. Sagan, H. Soder, N. Faure, J.-P. Colombier, M. Jourlin, and E. Audouard, Controlled nanostructrures formation by ultra fast laser pulses for color marking, Opt. Express **18**, 2913 (2010).

[69] G. D. Tsibidis, M. Barberoglou, P. A. Loukakos, E. Stratakis, and C. Fotakis, Dynamics of ripple formation on silicon surfaces by ultrashort laser pulses in subablation conditions, Phys. Rev. B **86**, 115316 (2012).

[70] C. Florian, S. V. Kirner, J. Krüger, and J. Bonse, Surface functionalization by laser-induced periodic surface structures, J. Laser Appl. **32**, 022063 (2020).

[71] G. Acosta, A. Reicks, M. Moreno, A. Borjali, C. Zuhlke, and M. Ghashami, Emissivity prediction of functionalized surfaces using artificial intelligence, J. Quant. Spectrosc. Radiat. Transfer **291**, 108325 (2022).

[72] H. Y. Wachman, The contributions of Lloyd Brewster Thomas, in *Rarefied Gas Dynamics: Technical Papers from the Proceedings of the Eighteenth International Symposium on Rarefied Gas Dynamics, University of British Columbia, Vancouver, British Columbia, Canada, July 26-30, 1992*, Vol. 158 (AIAA, Reston, VA, 1994), p. 461.

[73] S. C. Saxena and R. K. Joshi, Thermal accommodation and adsorption coefficients of gases, *CINDAS Data Series on Material Properties Group II, Properties of Special Materials*, II-1 (Hemisphere, London, 1989).

[74] H. Y. Wachman, The thermal accommodation coefficient: A critical survey, ARS J. **32**, 2 (1962).

[75] F. O. Goodman, Thermal accommodation, Prog. Surf. Sci. **5**, 261 (1974).

[76] C. Cercignani and C. D. Pagani, Rarefied flows in presence of fractionally accommodating walls, in *6th International Symposium on Rarefied Gas Dynamics*, edited by L. Trilling and H. Y. Wachman, Vol. 1 (Academic Press, New York, 1969), pp. 269–279.

[77] Z. M. Zhang, *Nano/Microscale Heat Transfer* (Springer, Berlin, 2020).

[78] A. A.-H. Hegazy, Thermal joint conductance of conforming rough surfaces: Effect of surface micro-hardness variation, Ph.D. thesis, University of Waterloo, Ontario, Canada, 2016.

[79] S. Song and M. Yovanovich, Correlation of thermal accommodation coefficient for engineering surfaces, ASME HTD **69**, 107 (1987).

[80] Y. Demirel and S. C. Saxena, Heat transfer in rarefied gas at a gas-solid interface, Energy **21**, 99 (1996).

[81] E. H. Kennard, *Kinetic Theory of Gases* (McGraw-Hill, New York, 1938).

[82] F. S. Sherman, A survey of experimental results and methods for the transition regime of rarefied gas dynamics, in *Rarefied Gas Dynamics: Proceedings of the Third International Symposium on Rarefied Gas Dynamics*, edited by J. A. Laurmann (Academic Press, Cambridge, 1963), Vol. 2, pp. 228–260 (1963).

[83] L. Lees and C.-Y. Liu, Kinetic-theory description of conductive heat transfer from a fine wire, Phys. Fluids **5**, 1137 (1962).

[84] G. S. Springer, Heat transfer in rarefied gases, in *Advances in Heat Transfer*, Vol. 7 (Elsevier, Amsterdam, 1971), pp. 163–218.

[85] M. M. R. Williams, A review of the rarefied gas dynamics theory associated with some classical problems in flow and heat transfer, Z. Angew. Math. Phys. **52**, 500 (2001).

[86] M. Hattori, S. Kosuge, and K. Aoki, Slip boundary conditions for the compressible Navier-Stokes equations for a polyatomic gas, Phys. Rev. Fluids **3**, 063401 (2018).

[87] G. V. Candler, Rate effects in hypersonic flows, Annu. Rev. Fluid Mech. **51**, 379 (2019).

[88] D. Y. Xu, A. Bilal, J. M. Zhao, L. H. Liu, and Z. M. Zhang, Near-field radiative heat transfer between rough surfaces modeled using effective media with gradient distribution of dielectric function, Int. J. Heat Mass Transf. **142**, 118432 (2019).

[89] S.-A. Biehs and J.-J. Greffet, Influence of roughness on near-field heat transfer between two plates, Phys. Rev. B **82**, 245410 (2010).